Machine learning reconstruction of shock-related optical phase aberrations utilizing de-focus irradiance patterns

Harrison C Bobbitt*, Thomas E DeFoor, Stanislav Gordeyev

University of Notre Dame, Notre Dame, IN, United States

ABSTRACT

High magnitude density gradients over the measurement aperture of aircraft-mounted optical sensors impose significant challenges for accurate wavefront measurement. Beams passing through these gradients experience a variety of aberrations ranging from piston and tip/tilt aberrations to higher order disturbances. The large magnitude optical-phase aberrations imposed by shock-waves have been shown to cause bifurcation of the focused irradiance pattern peaks in the observation plane, diminishing the effectiveness of wavefront sensing devices. By sensing aberrations in turbulent flow fields, system performance can be regained through the use of adaptive optics solutions which utilize a wavefront sensor to inform a phase correction. One wavefront sensor commonly used is the Shack-Hartmann wavefront sensor (SHWFS) which is composed of a micro-lens array that physically discretizes the incoming wavefront and is used for its simplicity and robustness. However, in the presence of shock-wave induced density gradients, the large optical phase shifts that arise impede this sensor's ability to accurately reconstruct wavefronts, leading to inaccurate phase correction. Previous research into shock-wave-tolerant, phase reconstruction algorithms for the SHWFS have shown that wavefront reconstruction is greatly assisted if the erroneous SHWFS tilt estimations are replaced with adapted estimates determined through machine learning methods, but were limited to non-unique mapping between simulated irradiance patterns and model phase estimation. As such, this paper explores use of de-focus irradiance patterns in combination with machine learning techniques to estimate the magnitude of optical phase aberrations over a range of discontinuity locations and orientations. The use of de-focus irradiance patterns allows for additional intensity structures to be extracted from aberration images, which encode phase-dependent structures that can be leveraged by machine learning algorithms for improved reconstruction. Developing an algorithm for estimating phase aberrations caused by shock-waves will aid in overall SHWFS performance in resolving highly aberrated wavefronts.

1. INTRODUCTION

Shock-waves, which are characteristic of many compressible flow environments, produce sudden changes in the freestream flow over short spatial distances. Accompanying this near-discontinuous change in flow properties is an abrupt increase in the local density, which can impose large magnitude variations in the optical-path length (OPL),[1,2] given by

$$OPL(x,y,t) = \int_0^z n(x,y,z,t)dz, \tag{1}$$

where n is the spatially and temporally varying index of refraction. The mean removed OPL, the optical path difference, OPD, commonly used in optical problems[3] is given by:

$$OPD(x,y,t) = OPL(x,y,t) - \langle OPL(x,y,t)\rangle_{\text{aperture}}, \tag{2}$$

which is related to the optical phase, ϕ, by:

$$\phi = (-2\pi/\lambda) * OPD, \tag{3}$$

where λ is the wavelength of the propagating laser light. Therefore, the propagation of light through a shock-wave will cause a change in optical phase, $\Delta\phi$. This change in optical phase degrades the performance of

Further author information:
E-mail: hbobbitt@nd.edu

Unconventional Imaging, Sensing, and Adaptive Optics 2026, edited by Jean Dolne, Santasri Bose-Pillai, Matthew Kalensky, Proc. of SPIE Vol. 14229, 1422911 · 2026 Published by SPIE
0277-786X · doi: 10.1117/12.3113679

many traditionally reliable aircraft-mounted optical propagation systems. To mitigate degrading effects of the shock-wave-induced ϕ variations, system performance can be retained through the use of adaptive optics (AO). AO systems typically consist of a wavefront sensor for measuring the phase aberration of the beam which then informs a phase correction. A traditionally reliable sensor used in AO applications is the Shack-Hartmann wavefront sensor (SHWFS). In practice, the SHWFS consists of a lenslet array which discretizes the incident light into focused irradiance patterns on a sensor. As such, aberrations in the phase of the incident light are reduced into a set of first-order aberrations (or tilts) over the aperture, which correspond to linear deviations of the sub-aperture focused irradiance patterns from their on axis positions on the sensor. By measuring the location of the displaced irradiance patterns, the local phase tilt can be measured using the focal length of the lenslets. The measured tilts are then used in a least-squares reconstruction algorithm to retrieve a spatially continuous estimate of the incident wavefront.[4] Proportionality between the centroid locations and the local tilts is required for this approach. However, Ref. 5 shows that optical phase discontinuities, $\Delta\phi$, induced by shock-waves do not follow this proportionality. Reference 5 proposed analytical relationships describing the effects of shock-waves in terms of optical path difference. In this work it was shown that high magnitude optical phase discontinuities on the spatial order of the lenslet size cause bifurcation and spreading of the beam. This results in the least-squares reconstruction to underestimate the change in OPD across the shock. By underestimating the OPD across the shock, $\Delta\phi$ is also underestimated. The behavior was experimentally verified in Ref. 6. Various studies have attempted to improve the performance of SHWFS in the presence of shock-waves through modifications to the reconstruction algorithm.[7–9] Reference 10,11 proposed the utilization of a machine learning technique to resolve the optical phase discontinuity magnitude. This work used an encoder style convolutional neural network (CNN), receiving a single-aperture irradiance pattern and returning a single estimate for $\Delta\phi$. Reference 10, 11 demonstrated the ability to accurately predict $\Delta\phi$, but the model saw diminished results in the presence of additive measurement noise, and could not resolve phase discontinuity magnitudes near 0 and 2π due to the modeling of the shock-wave as a step function. De-focus irradiance patterns have been used with SHWFS to improve the accuracy of traditional reconstruction by exploiting the extra information contained in the irradiance spot of a de-focus beam.[12,13] This study aims to continue the machine learning approach proposed in Ref. 10, 11, but using a ramp-modeled shock discontinuity and de-focus irradiance patterns. The utilization of de-focus patterns is proposed because the additional structures present may prove ideal for use in training a convolutional neural network. Convolutional neural networks have proven ideal for resolving complex visual structures,[14] so the additional structures in de-focus irradiance patterns may prove advantageous for improving a model's performance.

2. MACHINE LEARNING MODEL AND DATA GENERATION

2.1 CNN Architecture

A convolutional neural network (CNN) was used to identify the magnitude of optical phase discontinuities due to its proven effectiveness in image-based pattern recognition.[15,16] Pattern-recognition methods are well suited to this study because they can identify complex spatial features within irradiance patterns that are not captured by conventional centroid-based techniques. CNNs receive an array of pixel values corresponding to an image and process it using convolutional kernels that learn to identify relevant spatial features. Each kernel consists of a small matrix of trainable weights that is systematically moved across the input. At each location, the kernel weights are multiplied by the corresponding pixel values, and the resulting products are summed with a trainable bias term to produce a value in an output feature map. Each feature map indicates where a particular feature appears and how strongly it is present at each location. Because the same set of kernel weights is applied throughout the image, the network can detect a particular feature regardless of its spatial location. During training, the kernel weights and biases are iteratively adjusted through backpropagation to minimize the prediction error. Early convolutional layers typically learn simple features, such as edges, gradients, and localized intensity variations, while deeper layers combine these features to identify more complex structures within the irradiance pattern. The resulting feature maps are passed through nonlinear activation functions, which prevent successive layers from collapsing into a single linear transformation and enable the network to learn the complex, nonlinear relationships between image features and the target output. The feature maps are then processed by pooling layers, which reduce the spatial dimensions while retaining the most significant information. Finally, the

extracted features are flattened and passed to fully connected layers, which perform a regression task to estimate the optical phase discontinuity magnitude ($\Delta\phi$).

This study utilized the MATLAB Deep Learning Toolbox to construct, train, and evaluate the convolutional neural network. The input layer consisted of a 64×64 grayscale irradiance image, normalized by the maximum irradiance value within each image. The network employed three convolutional layers with 3×3 kernels and rectified linear unit (ReLU) activation functions to extract spatial features from the irradiance patterns. Following the first and second convolutional layers, 2×2 max-pooling layers were used to reduce the spatial dimensions of the feature maps while retaining the most significant information. The final convolutional layer produced a set of learned feature maps that were flattened and passed to a fully connected layer containing 32 neurons with ReLU activation. A final fully connected output layer generated a single regression output corresponding to the estimated optical phase discontinuity magnitude, $\Delta\phi$. Figure 1 shows the architecture of the CNN.

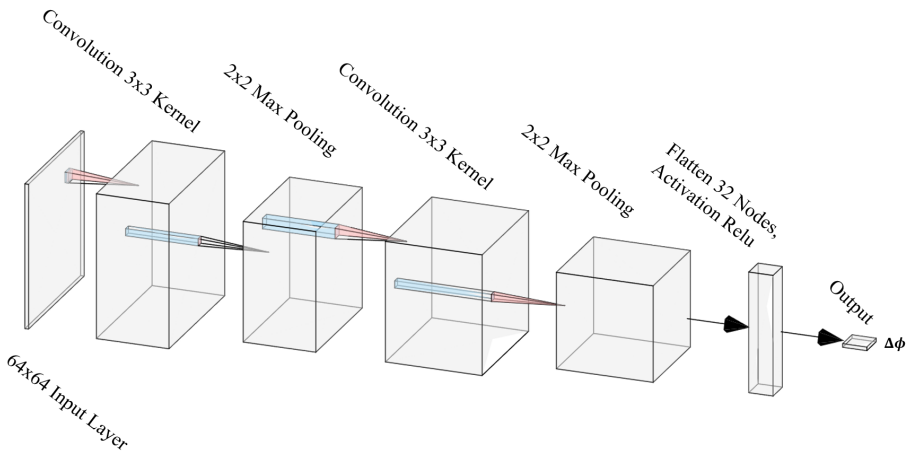


Figure 1: CNN architecture.

2.2 Data Generation

The irradiance patterns used for training and testing of the proposed CNN model were simulated by constructing a complex optical field to which a thin-lens transmittance function of focal length f was applied. This complex optical field was then propagated to the far-field by some distance z using fresnel transfer propagation. By modifying the optical phase function of the simulated beam before propagation, the location of the shock, Xs, the orientation of the shock, θ, and the strength of the discontinuity $\Delta\phi$ can be controlled. The irradiance patterns generated emulate a single sub-aperture of a SHWFS lenslet array.

The degree of de-focus present in the de-focus irradiance patterns is quantified by the Fresnel number,

$$N_f = \frac{a^2}{\lambda z}, \tag{4}$$

where λ is the wavelength of the beam, z is the distance from the pupil plane to the observation plane, and a is the characteristic size of the aperture (half width for square aperture). With a fixed a and λ, as z increases N_f decreases, resulting in a more normalized intensity distribution. As z decreases, N_f increases, generating a more distributed irradiance pattern. Thus the Fresnel number is an estimate of the distance away from the aperture considering the Fresnel approximation, where N_f values on the order of unity or greater generally correspond to the near-field Fresnel regime, in which wavefront curvature and propagation distance significantly influence the irradiance distribution. In contrast, $N_f << 1$ corresponds to the Fraunhofer regime, where the observation plane is sufficiently far from the aperture for the far-field approximation to apply.[17,18]

The equations used for propagating the simulated irradiance patterns are based on the Fresnel approximation for wave transfer:[19]

$$U_2(x,y) = \mathcal{F}^{-1}\{\mathcal{F}[U_1(x,y)]\ H(f_x,f_y)\}\,. \tag{5}$$

In this equation where $U_2(x,y)$ is the complex optical field after propagation and $U_1(x,y)$ is the source complex optical field containing phase and amplitude information in the form of:

$$U_1(x,y) = A_1(x,y)\,e^{i\phi_1(x,y)}, \tag{6}$$

where $A_1(x,y)$ is the amplitude of the source plane, $\phi_1(x,y)$ is the phase of the source plane, x, y are spatial coordinates, and i is the imaginary number unit. The Fresnel transfer function is defined by:

$$H(f_x,f_y) = e^{ikz}\ \exp\left[-i\pi\lambda z\left(f_x^2+f_y^2\right)\right], \tag{7}$$

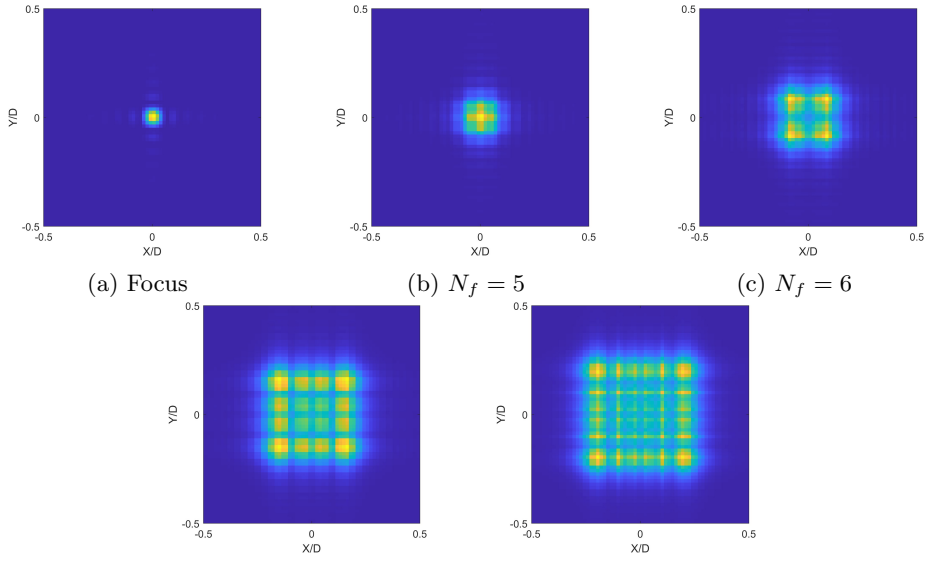
where k is the wavenumber, z is the defined propagation distance, λ is the laser's wavelength, and f_x, f_y are the spatial frequency coordinates. In Eq. 5, $\mathcal{F}$ and $\mathcal{F}^{-1}$ are the Fourier and inverse Fourier transforms respectively. By defining the propagation distance, the transfer equations simulate Fresnel diffraction of a wave to distance z. In addition to the transfer function, a lensing function has been elected to modify the beam transfer. The lensing function is used to simulate a single lenslet of a SHWFS. The lensing function is:

$$t_A(x,y) = \exp\left[-\,i\,\frac{k}{2f}\left(x^2+y^2\right)\right], \tag{8}$$

where f is the focal length of the defined lens. This modifies Eq. 5 as such:

$$U_2(x,y) = \mathcal{F}^{-1}\{\mathcal{F}[U_1(x,y)]\ H(f_x,f_y)t_A(x,y)\}\,. \tag{9}$$

With this useful modification, matching z and f results in a wave propagated to the focal length of a lens for the output plane, $U_2(x,y)$. By reducing z to a value less than f, de-focus irradiance patterns are generated with the degree of de-focus quantified by Eq. 4. Figure 2 presents an example of the focused irradiance pattern together with several de-focused cases generated using the Fresnel approximation for wave propagation. Compared with the focused case, the de-focused patterns contain a greater number of distinct spatial features and intensity variations. As the degree of de-focus, and consequently the Fresnel number, increases, these structures become more pronounced and complex. The additional spatial information may provide a machine-learning model with a richer set of features from which to identify relationships between the irradiance pattern and the underlying optical aberration.

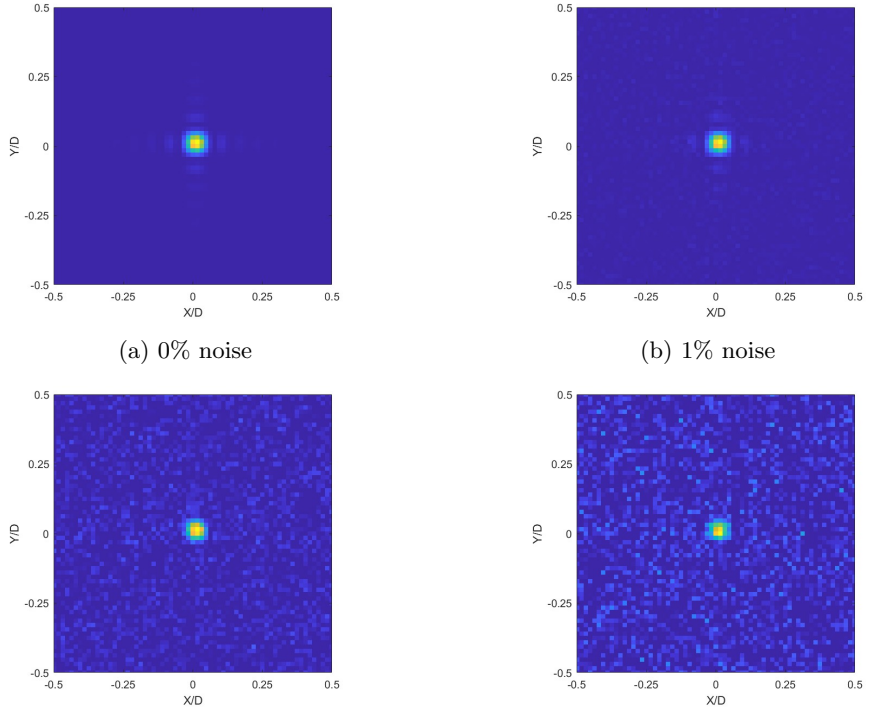


(a) Focus (b) $N_f = 5$ (c) $N_f = 6$

(d) $N_f = 8$ (e) $N_f = 10$

Figure 2: Simulated irradiance patterns for various N_f.

Additionally, it is desired to test the performance of the neural network with the presence of additive measurement noise. Noise levels of $0\%, 1\%, 5\%$, and 10% are shown in Fig. 3. As the noise level is increased the irradiance patterns become washed out relative to the nominal case with zero noise.



(a) 0% noise (b) 1% noise

(c) 5% noise (d) 10% noise

Figure 3: Example focused irradiance patterns with increasing levels of additive Gaussian noise.

For this study, the shock-wave is modeled as a ramp function optical phase discontinuity with varying ramp height corresponding to the magnitude of the aberration, $\Delta\phi$, varying shock location, Xs, and varying orientation on the aperture, θ (see Fig. 4). Changing X_s is important because the position of the discontinuity determines how much of the optical aperture is affected on either side of the shock. As the shock moves from the center toward the edge of the aperture, the relative areas associated with each phase region change, producing different diffraction structures and irradiance distributions. Similarly, varying θ changes the direction along which the phase discontinuity intersects the aperture, since the data is simulated using a square aperture rather than circle, this orientation changes the irradiance pattern. Because the aperture and sampled irradiance image have fixed spatial coordinates, rotating the discontinuity alters the orientation of the resulting intensity features. Including variations in both X_s and θ therefore prevents the model from relying on a single shock position or orientation and requires it to identify irradiance features that are fundamentally related to $\Delta\phi$. This improves the model's ability to estimate shock strength under the range of discontinuity geometries that may occur in practical aero-optical environments.

In addition to the phase discontinuity parameters, propagation distance of the simulated irradiance patterns is varied. This allows for irradiance patterns to be generated at de-focus planes. De-focus irradiance patterns have additional structures present which may allow for more accurate reconstruction. Although it is known irradiance drop-out may occur in the presence of sharp optical gradients[20] this consideration is not modeled. Data sets utilizing focus irradiance patterns are compared to those using de-focus patterns. A summary of the various parameters for incident wavefronts is shown in Fig. 4. This paper demonstrates the model's ability to discern $\Delta\phi$ in the presence of varying Xs, θ, and noise level for finite width optical aberrations.

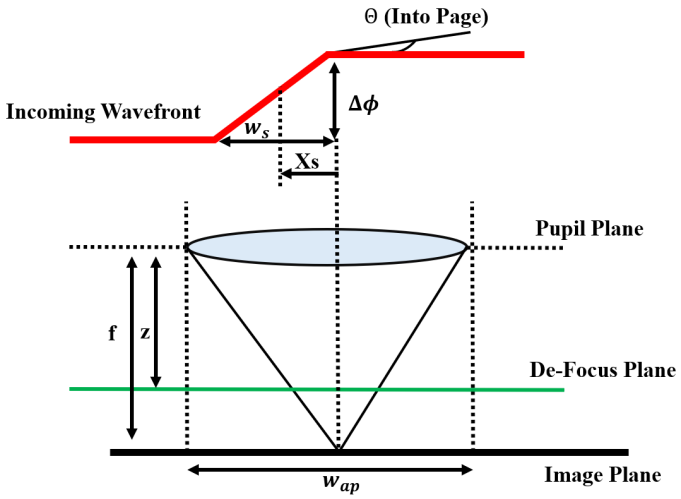


Figure 4: Schematic of incoming wavefront and its various parameters.

2.3 Simulated Data Validation

To validate the numerical irradiance-pattern simulations, the focused irradiance distribution generated by the wave-propagation model was compared with the analytical diffraction solution for a uniformly illuminated square aperture. This case provides a well-defined reference because its expected focal-plane irradiance distribution can be calculated directly, allowing the accuracy of the numerical focusing and propagation procedures to be evaluated before introducing more complex shock-induced phase distortions. The analytical solution is provided by:[21]

$$I(x,y) = \left(\frac{w_{ap}^2}{\lambda z}\right)^2 \operatorname{sinc}^2\left(\frac{w_{ap}x}{\lambda z}\right) \operatorname{sinc}^2\left(\frac{w_{ap}y}{\lambda z}\right). \tag{10}$$

By using identical values of aperture width w_{ap}, laser wavelength λ, and propagation distance z in Eq. 10 and in the numerical propagation procedure described by Eqs. 5–9, the resulting irradiance distributions can be directly compared. Agreement between the analytical and simulated patterns provides validation that the numerical wave-propagation model accurately reproduces the expected diffraction behavior of a uniformly illuminated square aperture. Figure 5 presents the simulated and analytical irradiance patterns, which exhibit close agreement in both the shape and spatial extent of the central diffraction lobe and the surrounding intensity structure. The comparison produces an RMSE of 6.984×10^{-4}, indicating that the difference between the normalized irradiance distributions is small. This close agreement supports the accuracy of the numerical implementation, including the applied focusing phase and wave-propagation procedure, and provides confidence in its use for simulating the more complex shock-induced phase distortions examined in this study.

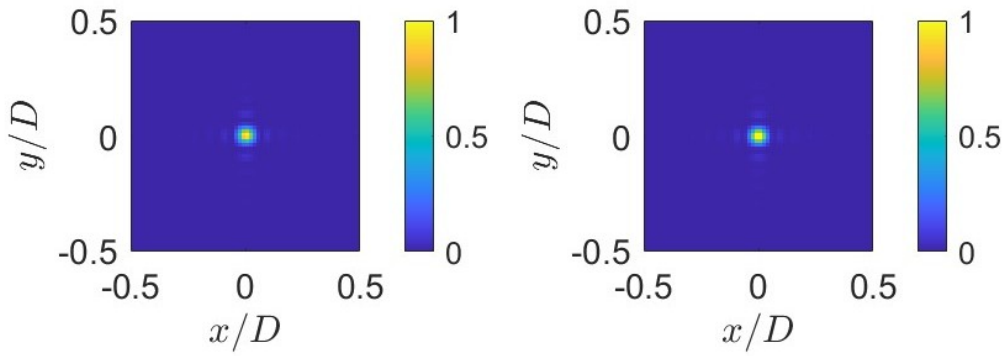


Figure 5: Comparison of simulated solution (Left) to analytical solution (right). RMSE: 6.984×10^{-4}

3. RESULTS

This section evaluates the performance of the neural network in estimating the strength of optical phase discontinuities from numerically generated irradiance patterns. Each dataset consist of 477,855 images, with each dataset randomly divided such that 80% of the images are used for training and the remaining 20% are reserved for testing. The generated irradiance patterns span a range of discontinuity locations, X_s, orientation angles, θ, and phase-discontinuity magnitudes, $\Delta\phi$, allowing the model to be evaluated across a broad range of optical conditions.

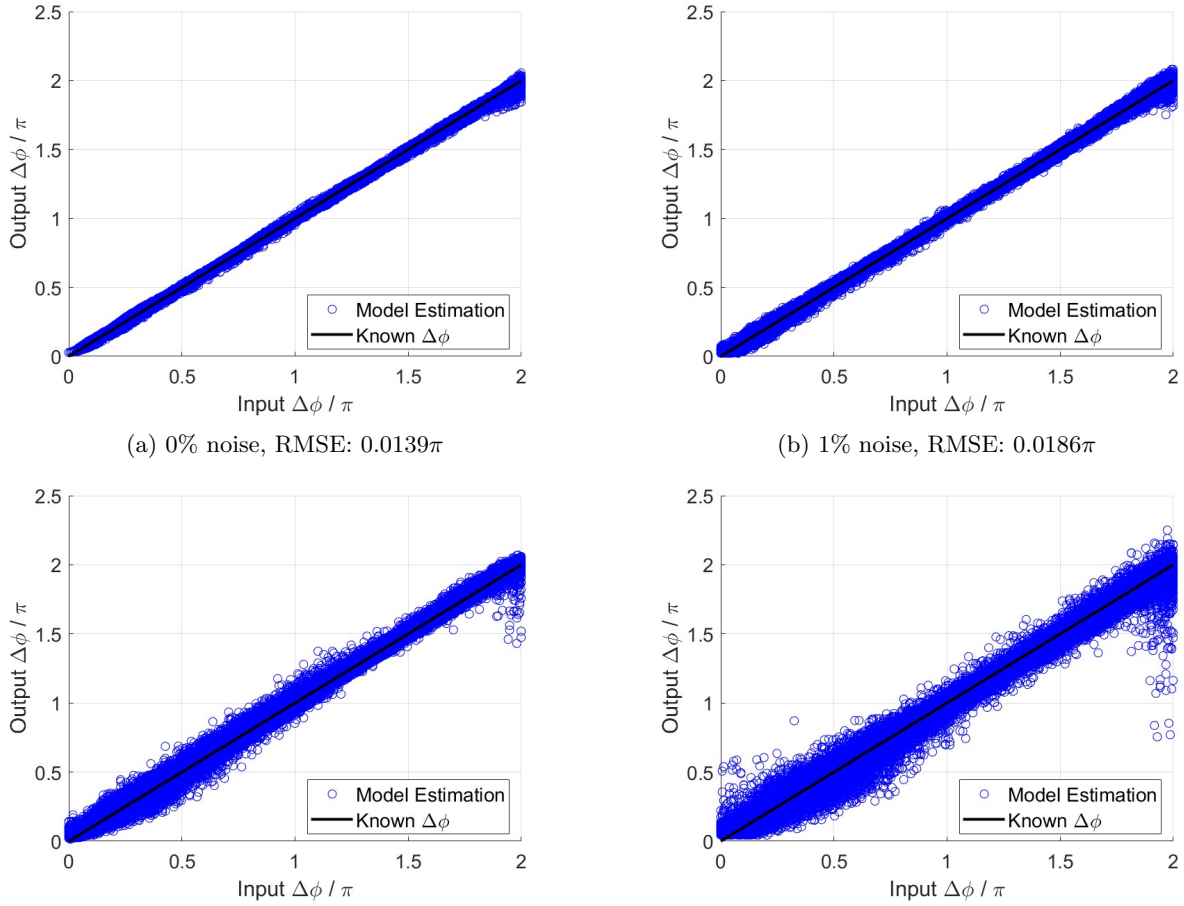
To assess the model's robustness to measurement degradation, the network is also tested using irradiance patterns containing additive noise levels of 1%, 5%, and 10% of the maximum irradiance value in each image. These tests are repeated for several Fresnel numbers, N_f, representing different degrees of de-focus. The resulting predictions are then compared with those obtained from the focused irradiance patterns to determine whether de-focus improves the network's ability to recover $\Delta\phi$, particularly under elevated noise conditions. The complete set of testing parameters is summarized in Table 1. For the highest N_f case, only 0% and 10% noise levels were examined as extreme cases. This is due to the trends identified when examining the other two cases and is discussed within the results.

Table 1: Training datasets for focused and de-focused irradiance cases with added noise.

Case	N_f	$\Delta\phi$	X_s	θ	Noise (%)
Focus	3.9	0–2π	0–0.4	0–360°	0, 1, 5, 10
De-focus	5	0–2π	0–0.4	0–360°	0, 1, 5, 10
De-focus	10	0–2π	0–0.4	0–360°	0, 10

3.1 Focus

This section outlines the results of the cases trained and tested with focused irradiance patterns ($N_f = 3.9$). These cases consisted of irradiance patterns with $\Delta\phi$ 0-2π with increments of 0.02, Xs 0-0.4 with increments of 0.01 and $\theta = 0 - 360°$ with increments of 10°. Additionally, the focused irradiance patterns are tested under noise levels of $0\%, 1\%, 5\%$, and 10%. The 477,855 images were split with 80% used in training and 20% used in testing. These results are shown in Fig. 6, where each of the noise levels are displayed.



(a) 0% noise, RMSE: 0.0139π

(b) 1% noise, RMSE: 0.0186π

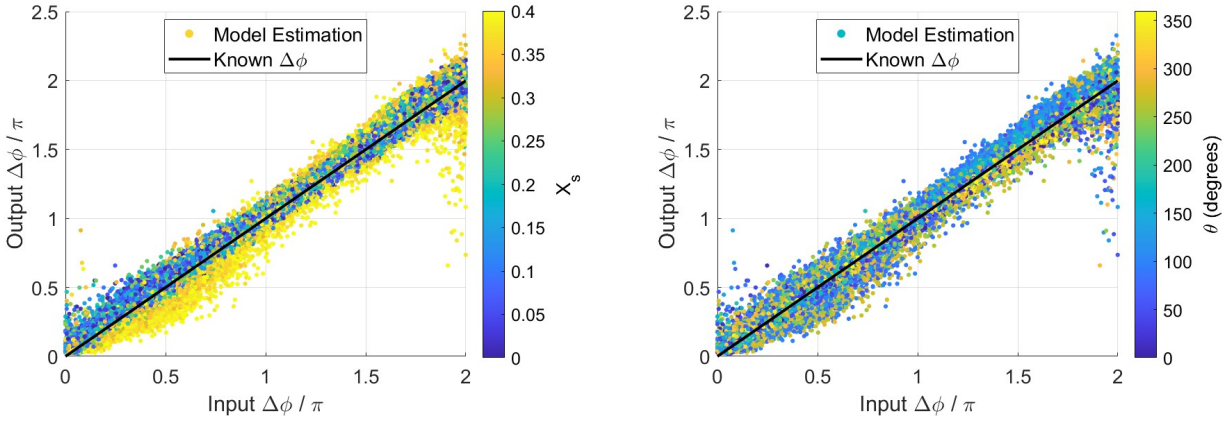
(c) 5% noise, RMSE: 0.0317π

(d) 10% noise, RMSE: 0.0520π

Figure 6: Model-predicted phase discontinuity compared with the known input $\Delta\phi$ for the $N_f = 3.9$ focus case at increasing noise levels.

The model is generally able to resolve the magnitude of the optical discontinuity for each of the noise levels with varying Xs and θ. The 0% and 1% noise cases seem more accurate, with the 1% case showing a slight spread comparatively. These two cases have comparable Root Mean Square Errors (RMSE) of 0.0139π for the no-noise case and 0.0186π for the 1% noise case. Error becomes more noticeable when looking at the 5% and 10% cases. Visually there is a greater spread of values from the known values, and there is a region towards the right side where predictions are less accurate than the rest of the plot. The 5% and 10% noise cases yield RMSE values of 0.0317π and 0.0520π, respectively, indicating greater dispersion about the known-value line than observed in the 0% and 1% noise cases. These results demonstrate an initial trend in which increasing noise degrades the accuracy and consistency of the model predictions. At the higher noise levels, the predictions exhibit both a broader spread and a greater occurrence of outliers, suggesting that the irradiance features used to estimate $\Delta\phi$ become increasingly obscured as the noise level increases.

To investigate the sources of prediction error in the 10% noise case, additional scatter plots were generated in which the data points were colored according to their corresponding X_s and θ values. Figure 7 presents these plots, allowing potential relationships between model error, shock location, and shock orientation to be identified.



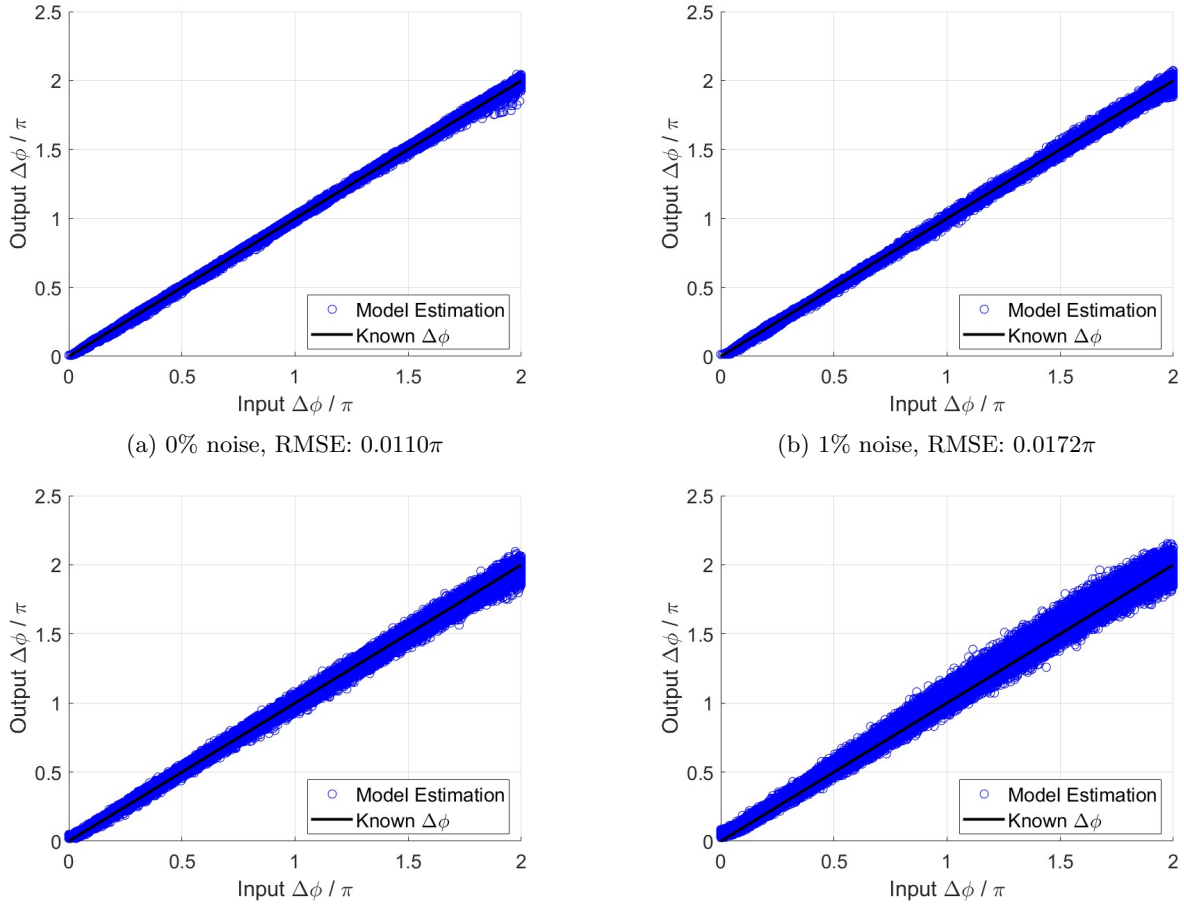
(a) (b)

Figure 7: Colored model performance showing Xs and θ for the focus 10% noise case.

Examining first the X_s-colored scatter plot in Fig. 7(a), the yellow data points have a tendency to underestimate $\Delta\phi$, especially at the upper right section of the plot. These points correspond to larger values of X_s, indicating that the shock is located closer to the edge of the aperture. In this configuration, a smaller portion of the shock-induced phase structure may remain within the aperture, reducing the spatial information available to the model. A systematic dependence on shock location is also visible on the left side of the plot, where cases with lower X_s, corresponding to shocks near the center of the aperture, tend to overestimate the discontinuity magnitude. In contrast, cases with higher X_s, corresponding to shocks farther from the center, tend to underestimate it. This separation suggests that shock location influences the direction of the model's prediction error, particularly as the discontinuity approaches the aperture boundary. Next, the dependence on θ is examined in Fig. 7(b). Unlike the X_s-colored results, the prediction errors do not exhibit an obvious clustering or systematic variation with shock orientation. Instead, the θ values appear to be distributed relatively uniformly throughout the prediction spread and among the outliers. This suggests that shock orientation has a weaker influence on the observed errors than shock location. However, the plot alone does not demonstrate that θ has no effect; rather, it indicates that no clear dependence on θ is apparent from this visualization.

3.2 De-Focus

This section outlines the performance of the model using the same optical discontinuity parameters as the focus cases, but employing de-focus irradiance patterns. The first set of irradiance patterns shown in Fig. 8 utilized a Fresnel Number of $N_f = 5$.



(a) 0% noise, RMSE: 0.0110π

(b) 1% noise, RMSE: 0.0172π

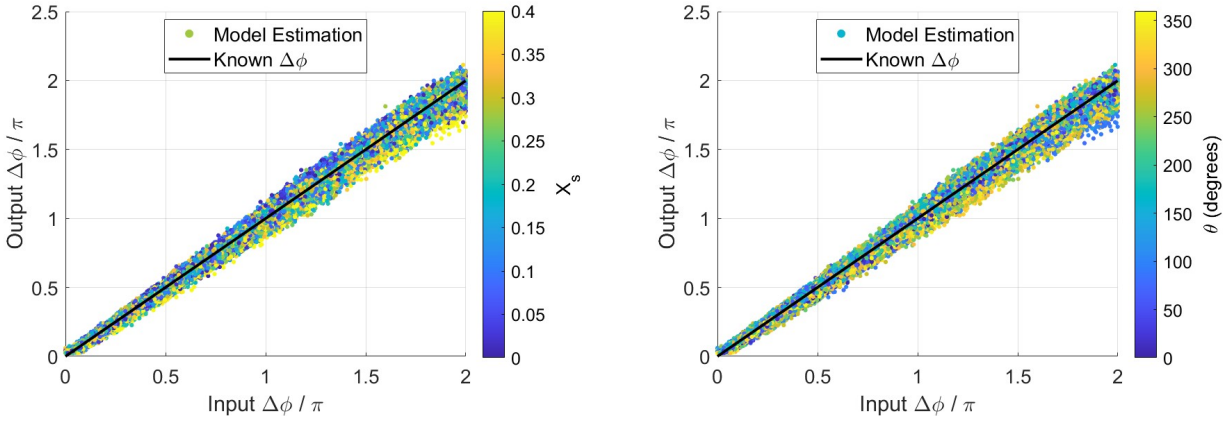
(c) 5% noise, RMSE: 0.0262π

(d) 10% noise, RMSE: 0.0534π

Figure 8: Model-predicted phase discontinuity compared with the known input $\Delta\phi$ for the $N_f = 5$ de-focus case at increasing noise levels.

As shown previously, the model is generally able to resolve $\Delta\phi$ despite variations in both X_s and θ. For the 0% and 1% noise cases, the prediction accuracy is comparable to that of the focused irradiance case with RMSE values of 0.0110π and 0.0172π respectively indicating a tighter spread from the known-value line. However, more noticeable differences emerge at the 5% and 10% noise levels. For the 5% noise case, the de-focus model achieved a lower RMSE of 0.0262π than the focused case shown in Fig. 6(c), indicating a tighter distribution of predictions about the known-value line. In addition to the reduced spread, the outliers visible on the right side of Fig. 6(c) are absent in the de-focus case. This suggests that the additional spatial information contained within the de-focus irradiance patterns improves the model's ability to estimate $\Delta\phi$. For the 10% noise case, the $N_f = 5$ model produced an RMSE of 0.0534π, which is slightly higher than that of the focused case shown in Fig. 6(d). Despite the higher RMSE, a visual comparison reveals substantially fewer outlier predictions for the $N_f = 5$ case. Additionally, each of the different noise levels for the $N_f = 5$ cases exhibit fewer visually apparent outliers. This indicates that the de-focus model may provide more consistent predictions under high-noise conditions, even when the overall RMSE does not show a corresponding improvement.

Next the sources of error were investigated as before in the focus case. Figure 9 shows colored scatter plots displaying Xs and θ for the $N_f = 5$, 10% noise case.

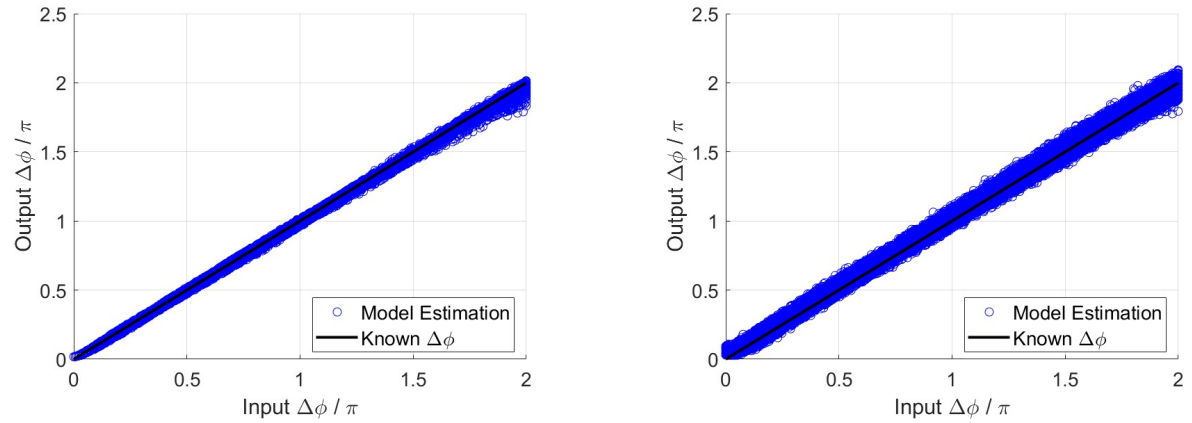


(a) (b)

Figure 9: Colored model performance showing Xs and θ for the $N_f = 5$, 10% noise case.

Unlike the focused case, the X_s and θ-colored scatter plots exhibit a largely uniform distribution, with no clear clustering of prediction errors according to either parameter. This suggests that the de-focus irradiance patterns reduce the model's sensitivity to shock location and orientation. The broader spatial distribution of information in the de-focus patterns likely allows relevant features associated with $\Delta\phi$ to remain identifiable across a wider range of X_s and θ, thereby producing more consistent predictions.

An additional two data sets were constructed utilizing de-focus irradiance patterns with a Fresnel Number $N_f = 10$. Only the noise levels of 0% and 10% are examined here with the same variations of $\Delta\phi$, Xs, and θ. These noise levels were selected because they represent the two extremes of the dataset and allow the model's performance under ideal and highly degraded conditions to be compared directly. Additionally, the trend observed in the previous cases suggests that an increase in N_f improves the models accuracy by introducing additional spatial structures in the irradiance patterns. The minimum and maximum noise cases for the final data set are displayed in Fig. 10.



(a) 0% noise, RMSE: 0.0157π (b) 10% noise, RMSE: 0.0348π

Figure 10: Model estimation of $\Delta\phi$ compared with the known $\Delta\phi$ for de-focused irradiance patterns at $N_f = 10$ with varying noise levels.

The model trained using $N_f = 10$ irradiance patterns accurately resolves the optical-discontinuity magnitude in both the zero-noise and 10% noise cases. Comparing the zero-noise results in Figs. 6(a), 8(a), and 10(a), all three models demonstrate a similar ability to recover $\Delta\phi$. Although the $N_f = 10$ case has the highest RMSE at

0.0157π, the predictions remain closely distributed about the known-value line, indicating that the underlying relationship is still resolved accurately. A more substantial improvement is observed for the 10% noise case shown in Fig. 10(b), where the $N_f = 10$ model achieves an RMSE of 0.0348π. This value is lower than those obtained for the corresponding maximum-noise focused and $N_f = 5$ cases shown in Figs. 6(d) and 8(d), respectively. In addition to the reduction in RMSE, the $N_f = 10$ predictions do not exhibit the prominent outliers observed in the focused case. The reduced prediction spread suggests that the additional spatial features present in the more highly de-focused irradiance patterns help preserve information related to $\Delta\phi$ when the images are degraded by noise. Overall, these results indicate that increasing the degree of de-focus may improve the robustness and reliability of CNN-based optical-discontinuity estimation under noisy measurement conditions.

As before, the highest noise case is examined for relationships between the model accuracy, Xs, and θ. Figure 11 shows the colored scatter plots for the $N_f = 10$ case with 10% noise.

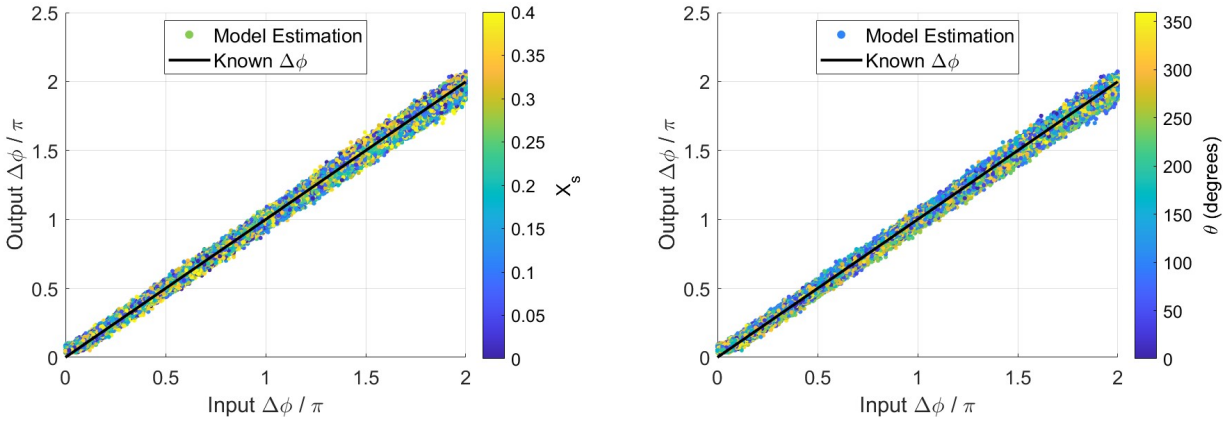


Figure 11: Colored model performance showing Xs and θ for the $N_f = 10$, 10% noise case.

As observed for the $N_f = 5$, 10% noise case, the data points exhibit a substantially more uniform distribution, with no clear dependence of the prediction errors on either X_s or θ. This supports the conclusion that the broader spatial distribution of de-focus irradiance patterns allows features associated with $\Delta\phi$ to remain identifiable regardless of Xs and θ.

4. CONCLUSION

This paper investigated the ability of a convolutional neural network to estimate the magnitude of an optical-phase discontinuity from 64×64 irradiance images under a range of conditions. Optical-aberration parameters, such as degree of de-focus (quantified by the Fresnel number N_f), and level of additive noise were systematically varied to evaluate the robustness of the model. The network was trained and validated using simulated data and demonstrated a strong ability to recover $\Delta\phi$ across most test conditions. However, as the noise level increased, the model trained using focused irradiance patterns experienced a decline in performance. In contrast, models using de-focused irradiance patterns produced more accurate and consistent estimates at higher noise levels, especially in mitigation of outlier predictions. The results further indicated that performance improved as the degree of de-focus increased, suggesting that de-focused measurements contain additional spatial information that enhances the model's ability to resolve $\Delta\phi$ in noisy environments. Additionally, the use of de-focus irradiance patterns mitigates the dependence of prediction error of $\Delta\phi$ on the shock location as observed in the focus case. By distributing optical information across a broader region of the aperture, the de-focus patterns seem to preserve identifiable features resistant to noise degradation or approaching the edge of the aperture. This results in less outlier predictions and a more uniform distribution of errors with respect to Xs and θ.

This study demonstrates the potential of convolutional neural networks for estimating optical-phase discontinuity magnitude in conditions where conventional wavefront-sensing and reconstruction methods may become

unreliable. In particular, the improved performance observed for de-focused irradiance patterns at elevated noise levels suggests that de-focus can preserve or introduce spatial features that are useful for identifying $\Delta\phi$. These results support the development of machine-learning-based approaches for shock-tolerant wavefront sensing and other optical measurements involving sharp phase variations.

Future work should expand the training and testing space to include a wider range of discontinuity characteristics, such as varying discontinuity width and modeling function. Additional optical aberrations and more realistic noise sources should also be considered to better represent practical measurement environments. The influence of system parameters, including aperture geometry, propagation distance, wavelength, detector resolution, and degree of de-focus, should be further examined to determine how well the model generalizes across different optical configurations. Finally, the method should be validated using experimentally collected irradiance data and, ultimately, measurements obtained in the presence of shock-waves. Such validation would provide a more rigorous assessment of the model's robustness and its suitability for implementation in practical wavefront-sensing systems.

ACKNOWLEDGMENTS

The authors would like to acknowledge the use of generative AI in the editing of grammar and readability for this paper.

REFERENCES

[1] J. Morrida, S. Gordeyev, N. De Lucca, and E. J. Jumper, "Shock-related effects on aero-optical environment for hemisphere-on-cylinder turrets at transonic speeds," *Applied Optics* **56**(16), pp. 4814–4824, 2017.

[2] J. Panda and G. Adamovsky, "Laser light scattering by shock waves," *Physics of Fluids* **7**(9), pp. 2271–2279, 1995.

[3] S. Gordeyev, E. J. Jumper, and M. R. Whiteley, *Aero-Optical Effects: Physics, Analysis and Mitigation*, Wiley Series in Pure and Applied Optics, John Wiley & Sons, Inc., Hoboken, NJ, 1st ed., 2023.

[4] D. L. Fried, "Least-square fitting a wave-front distortion estimate to an array of phase-difference measurements," *Journal of the Optical Society of America* **67**, pp. 370–375, Mar. 1977.

[5] M. Kalensky, M. R. Kemnetz, and M. F. Spencer, "Effects of shock waves on shack–hartmann wavefront sensor data," *AIAA Journal* **61**, pp. 2356–2368, June 2023.

[6] M. R. Kemnetz, M. Kalensky, T. E. DeFoor, and M. F. Spencer, "Experimental investigation into the effects of shock waves on Shack–Hartmann wavefront sensor measurements," in *Unconventional Imaging, Sensing, and Adaptive Optics 2023*, **12693**, pp. 353–364, SPIE, Oct. 2023.

[7] E. D. Chu, T. J. Bukowski, and S. Gordeyev, "Improved wavefront reconstruction for Shack–Hartmann wavefront sensor in the presence of shock-related distortions," *Optics & Laser Technology* **187**, p. 112764, 2025.

[8] T. E. DeFoor, M. Kalensky, M. R. Kemnetz, T. J. Bukowski, and M. F. Spencer, "Shock-wave-tolerant phase reconstructor for the Shack–Hartmann wavefront sensor," in *Unconventional Imaging, Sensing, and Adaptive Optics 2023*, **12693**, pp. 228–236, SPIE, Oct. 2023.

[9] T. E. DeFoor, T. J. Bukowski, M. Kalensky, and S. Gordeyev, "Experimental measurements and compensation of optical phase discontinuities," in *Unconventional Imaging, Sensing, and Adaptive Optics 2025*, **13619**, p. 136190O, SPIE, Sept. 2025.

[10] T. E. DeFoor, T. J. Bukowski, M. Kalensky, and S. Gordeyev, "Phase discontinuity classification from single-aperture irradiance patterns using machine learning," in *Unconventional Imaging, Sensing, and Adaptive Optics 2024*, J. J. Dolne, S. R. Bose-Pillai, and M. Kalensky, eds., **13149**, p. 131490F, SPIE, 2024.

[11] T. E. DeFoor, T. J. Bukowski, M. Kalensky, and S. Gordeyev, "Machine learning approach to estimating optical-phase discontinuities using single-aperture irradiance patterns," *Applied Optics* **64**, pp. 9202–9214, Nov. 2025.

[12] C. Li, B. Li, and S. Zhang, "Phase retrieval using a modified Shack–Hartmann wavefront sensor with defocus," *Applied Optics* **53**(4), pp. 618–624, 2014.

[13] F. Feng, C. Li, and S. Zhang, "Moment-based wavefront reconstruction via a defocused Shack–Hartmann sensor," *Optical Engineering* **57**(7), p. 074106, 2018.

[14] A. Géron, *Hands-On Machine Learning with Scikit-Learn, Keras, and TensorFlow: Concepts, Tools, and Techniques to Build Intelligent Systems*, O'Reilly Media, Sebastopol, CA, 2nd ed., 2019.

[15] A. Krizhevsky, I. Sutskever, and G. E. Hinton, "ImageNet classification with deep convolutional neural networks," in *Advances in Neural Information Processing Systems*, **25**, pp. 1097–1105, Curran Associates, Inc., 2012.

[16] K. O'Shea and R. Nash, "An introduction to convolutional neural networks," *arXiv preprint arXiv:1511.08458* , 2015.

[17] R. K. Tyson, *Principles and Applications of Fourier Optics*, IOP Publishing, Bristol, UK, 2014.

[18] J. W. Goodman, *Introduction to Fourier Optics*, McGraw-Hill, New York, 2nd ed., 1996.

[19] J. D. Schmidt, *Numerical Simulation of Optical Wave Propagation with Examples in MATLAB*, vol. PM199 of *SPIE Press Monograph*, SPIE Press, Bellingham, WA, 2010.

[20] S. Gordeyev, J. A. Cress, and E. J. Jumper, "Far-field laser intensity drop-outs caused by turbulent boundary layers," *Journal of Directed Energy* **5**(1), pp. 58–75, 2013.

[21] P. H. Merritt and M. F. Spencer, *Beam Control for Laser Systems*, Directed Energy Professional Society, Albuquerque, NM, 2nd ed., 2018.